PHOTONICS Research

High-speed PGC demodulation model and method with subnanometer displacement resolution in a fiber-optic micro-probe laser interferometer

Yisi Dong,[1,2] Wenwen Li,[1,2] Jinran Zhang,[1,2] Wenrui Luo,[1,2] Haijin Fu,[1,2,4] Xu Xing,[1,2,5] Pengcheng Hu,[1,2] Yongkang Dong,[3] and Jiubin Tan[1,2]

[1]Center of Ultra-precision Optoelectronic Instrument, Harbin Institute of Technology, Harbin 150080, China
[2]Key Laboratory of Ultra-precision Intelligent Instrumentation (Harbin Institute of Technology), Ministry of Industry and Information Technology, Harbin 150080, China
[3]National Key Laboratory of Science and Technology on Tunable Laser, Harbin Institute of Technology, Harbin 150001, China
[4]e-mail: haijinfu@hit.edu.cn
[5]e-mail: Xingxu@hit.edu.cn

Received 20 November 2023; revised 3 February 2024; accepted 15 February 2024; posted 15 February 2024 (Doc. ID 513576); published 1 May 2024

As the key of embedded displacement measurement, a fiber-optic micro-probe laser interferometer (FMI) is of great interest in developing high-end equipment as well as precision metrology. However, conventional phase-generated carrier (PGC) approaches are for low-speed scenes and local error analysis, usually neglecting the global precision analysis and dynamic effect of system parameters under high-speed measurement, thus hindering their broad applications. We present a high-speed PGC demodulation model and method to achieve subnanometer displacement measurement precision in FMI. This model includes a global equivalent resolution analysis and revelation of the demodulation error mechanism. Utilizing this model, the failure issues regarding the PGC demodulation method under high speed and large range are addressed. Furthermore, an ultra-precision PGC demodulation algorithm based on the combination of static and dynamic delay adaptive regulation is proposed to enable high-speed and large-range displacement measurement. In this paper, the proposed model and algorithm are validated through simulation and experimental tests. The results demonstrate a displacement resolution of 0.1 nm with a standard deviation of less than 0.5 nm when measuring at a high velocity of 1.5 m/s—nearly a tenfold increase of the latest study. © 2024 Chinese Laser Press

https://doi.org/10.1364/PRJ.513576

1. INTRODUCTION

With the rapid development of high-end equipment manufacturing and the widespread adoption of photoelectric detection technology, laser interferometric displacement measurement technology [1] has emerged as a crucial tool in the realm of ultra-precision machining. This technology offers distinct advantages, such as high precision, non-contact measurement, and traceability [2]. Traditional mirror-based laser interferometers, while highly precise, often exhibit large physical footprints and demand stringent measurement environments. In contrast, embedded fiber-optic micro-probe laser interferometers (FMIs) characterized by their small size, high integration, robust environmental adaptability, and online measurement capabilities, play an important role in confined measurement environments and subnanometer resolution measurement [3–5].

The performance of FMI is largely limited by demodulation technology. As a mature technology, white light interferometers, utilizing broadband light sources for cavity length measurement, can achieve subnanometer resolution [6]. However, this remarkable resolution is primarily suitable for quasi-static measurements and may not perform optimally in high-speed measurements. Consequently, the quadrature intensity demodulation technique [7,8] has gained popularity for fast measurements, yet it is constrained by a limited dynamic range ($\lambda/4$), which brings limitations in practical applications. In addition to the above-mentioned methods, phase-generated carrier (PGC) technology offers advantages including good linearity, broad dynamic range, and high sensitivity, making it a widely adopted signal demodulation technology [9,10].

Typically, the maximum measurement speed of the interferometer is limited by the laser modulation frequency [11]. PGC technology needs to generate a high-frequency carrier phase signal based on the modulated laser frequency and the idle length of the interferometer, so as to be applied to high-speed measurement. He *et al.* proposed an inverse tangent differential self-crossing algorithm (PGC-Arctan-DSM), which attains a

signal-to-noise-and-distortion (SINAD) of 60 dB [12]. In 2021, Yan *et al.* proposed a nonlinear error compensation method based on the PGC-Arctan algorithm to eliminate the nonlinear errors of nanoscale displacement measurements [13]. In 2022, Chen *et al.* introduced a demodulation scheme that combines PGC-Arctan and PGC-DCM to reduce nonlinear errors from 3.65 nm to 0.10 nm at a displacement of 1 μm/s [14]. The same year, Li *et al.* presented an enhanced PGC demodulation algorithm based on frequency mixing and division difference [15]. Compared to traditional PGC-DCM and PGC-Arctan algorithms, this method improves the signal-to-noise ratio (SNR) by 26.26 dB and 35.66 dB, respectively. However, all these methods analyze the signal quality of the demodulation results and do not directly establish a relationship between PGC system performance and displacement measurement resolution, thus lacking a basis for subnanometer resolution design. Furthermore, the optimization algorithms for PGC are designed for short-distance and low-speed measurement conditions, and a high-speed PGC demodulation model with subnanometer precision has not been established and realized.

At present, the primary factors affecting PGC demodulation include accompanied optical-intensity modulation (AOIM), phase modulation depth (PMD), and carrier phase delay (CPD), making further enhancement of interferometer demodulation precision challenging. In the existing technology, errors arising from AOIM and PMD have been effectively mitigated [16–20], while errors caused by CPD remain difficult to suppress, and even the displacement signal cannot be demodulated successfully under high-speed and long-distance measurement conditions. To address this, more suitable solutions, such as the elliptic fitting method, have been proposed [21,22]. However, this approach has the drawbacks of substantial computational requirements and slow operation speed and is generally used for off-line measurements. In contrast, the eigenvalue extremum method, based on the elliptic fitting algorithm, enables real-time online measurement. Nevertheless, its limitation lies in its limited sampling rate, making it challenging to extract accurate extremum values under conditions of slow sampling rates. Furthermore, the elliptic fitting algorithm may fail when the Lissajous diagram of the system forms a straight line.

To address the above-mentioned CPD-related issues, Dong *et al.* [23] proposed a CPD prediction method. However, this method is a static prediction of CPD, which cannot meet the dynamic measurement requirements. In response to this problem, Wang *et al.* [24] employed the Arctan algorithm in PGC to estimate the real-time carrier phase delay compensation amount, but when the phases to be measured correspond to integer multiples of π, the demodulation results exhibit discontinuities. Then Xie *et al.* [25] proposed a CPD extraction method that effectively avoids the above problem, but also brings a new problem, that is, when the CPDs correspond to odd multiples of $\pi/4$, the demodulation results exhibit discontinuities. These jump points significantly affect modulation accuracy, highlighting the need for reliable and effective online CPD compensation under high-speed and large-range measurement conditions.

This paper introduces a resolution equivalent model based on the PGC-Arctan demodulation algorithm with internal modulation. This model effectively represents the PGC demodulation process as a signal acquisition system that includes equivalent error terms. It establishes a relationship between the effective number of bits N^* in the equivalent model and the actual precision of the demodulation system. This approach allows for confident error allocation in the design of FMIs, offering valuable guidance for this type of design. Furthermore, the paper conducts a theoretical analysis of phase demodulation errors that occur in traditional PGC algorithms under high-speed and large-range measurement conditions. In such scenarios, issues like characteristic parameter disappearance and system CPD cannot be ignored, as CPD has a significant impact on the calculation results. Therefore, an adaptive compensation algorithm, combining dynamic and static CPD, is designed. Experimental results demonstrate that using this compensation algorithm, measurement errors caused by CPD can be reduced to less than 0.5 nm at a measurement speed of 1.5 m/s, meeting subnanometer level resolution precision requirements.

The subsequent sections of this paper are organized as follows. In Section 2, the whole work of this paper is introduced. In Section 3, an equivalent model for subnanometer precision resolution using the PGC demodulation algorithm under high-speed measurement is established. Furthermore, the relationship between the performance of the demodulation system and the equivalent model parameters is highlighted. Additionally, the influence of CPD, AOIM, and PMD on the demodulation results is analyzed, while offering reasonable solutions based on the underlying generation mechanism. In Section 4, the impact of CPD on the quality of demodulation signals is assessed through simulations, and a high-precision delay dynamic adaptive PGC demodulation algorithm is designed. Finally, the feasibility and advanced nature of this method are validated through comparative experiments.

2. RESULTS AND SUMMARY OF HIGH-SPEED AND HIGH-PRECISION PGC DEMODULATION

The overall context of this paper is shown in Fig. 1. A novel resolution-equivalent model is proposed for the first time to evaluate the accuracy of displacement measurement, based on the measurement concept of FMI and the operating principle of the PGC demodulation algorithm. After analyzing the error terms of each link in FMI, aiming at the nonlinear error introduced by the CPD phenomenon under high-speed measurement, a high-precision PGC demodulation algorithm with delay dynamic adaptive regulation is proposed for the first time.

In Fig. 1, the lower-left corner represents the overall actual hardware platform structure containing the optical path and circuitry, and the gray block diagram in the upper-left corner is its equivalent structure. Combining these two structure diagrams, it can be seen that in this paper, the overall structure is equivalent to an analog-to-digital converter (ADC) containing each error term, whose input is the phase to be measured φ_0, and the output is the calculated phase φ', and based on this equivalence process, a resolution equivalent model is established for evaluating the accuracy of the FMI displacement

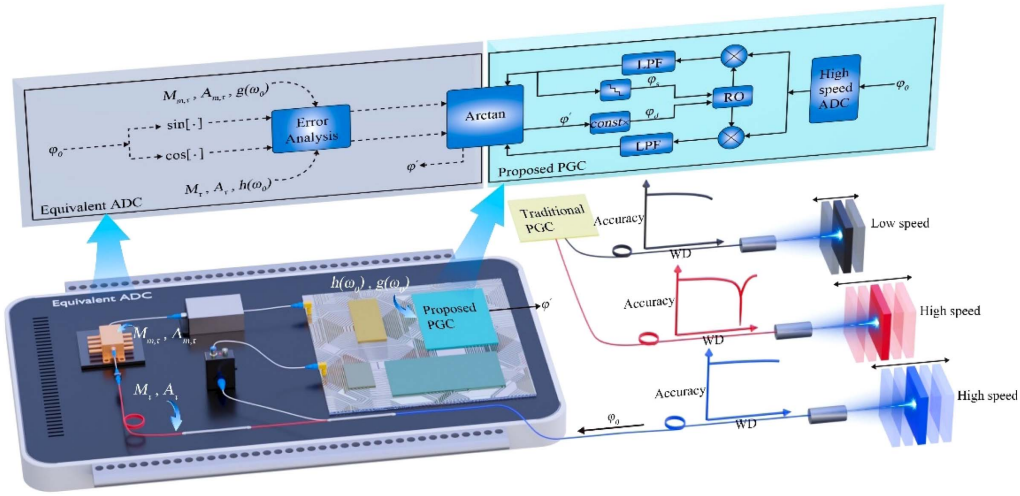

Fig. 1. System schematic of a PGC demodulation model and method with high-speed and high-precision performance.

measurement. From the results of the equivalence, integrate all the errors and noise in the FMI system and consider them as the quantization errors of the equivalent ADC. Put simply, the accuracy of the displacement measurement of FMI can be quantified by the effective number of bits of the equivalent ADC.

Then, analyze the error terms introduced by each error source in the measurement system, such as the error terms M_τ and A_τ introduced by the CPD phenomenon, and establish the phase demodulation error model according to the errors existing in FMI. The phenomenon of PGC not working properly under high-speed measurement is revealed initially, and simultaneously, the CPD phenomenon is found to be the key reason limiting the further improvement of displacement measurement accuracy under high-speed measurement. Hence, a high-precision PGC demodulation algorithm with delay dynamic adaptive regulation is designed. This algorithm is depicted in the blue algorithm block diagram located in the upper-right corner.

Finally, following experimental analysis, the comparison graphs of displacement measurement accuracy between high-speed and low-speed, traditional PGC methods [24,25] and the proposed PGC method are plotted in gray, red, and blue in the lower-right corner. From these three depicted accuracy versus work distance curves, it can be seen that with the increasing measurement speed, traditional PGC methods exhibit curve distortion due to the CPD phenomenon, while the proposed PGC method still has high measurement accuracy at the same high measurement speed, realizing a displacement resolution of 0.1 nm with a standard deviation of less than 0.5 nm at a speed of 1.5 m/s.

3. HIGH-SPEED PGC DEMODULATION MODEL FOR SUBNANOMETER PRECISION

A. Equivalent Analysis Methods for Deep Subnanometer Resolution

Figure 2 illustrates the block diagram of the PGC demodulation algorithm based on FMI. This paper presents an FMI, characterized by its small size, common optical path, and easy integration. The phase to be measured, $\varphi_0(t) = 4\pi n \cdot L_0(t)/\lambda$, is directly proportional to the displacement to be measured, $L_0(t)$, where n is the refractive index and λ is the output wavelength of the laser. The input signal passes through the FMI, photodetector, and high-speed analog-to-digital converter (ADC) to create an interference signal, which then enters the PGC demodulation system for signal processing. The PGC algorithm can be regarded as a combination of two lock-in amplifiers and an Arctan algorithm, and the specific demodulation process unfolds as follows: the collected interference signal splits into two channels, and both interference signals are simultaneously multiplied by the first and second harmonic

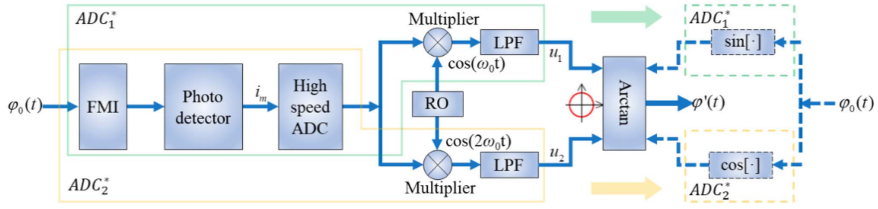

Fig. 2. Block diagram of the FMI demodulation system based on the PGC algorithm. FMI: fiber-optic micro-probe laser interferometer; RO: reference oscillator; LPF: low-pass filter; Arctan: inverse tangent algorithm. The left side of the Arctan algorithm represents the actual interference setup, while the right side shows the equivalent diagram. The green and yellow wireframes on both sides correspond to the equivalent ADC_1^* and ADC_2^*, respectively.

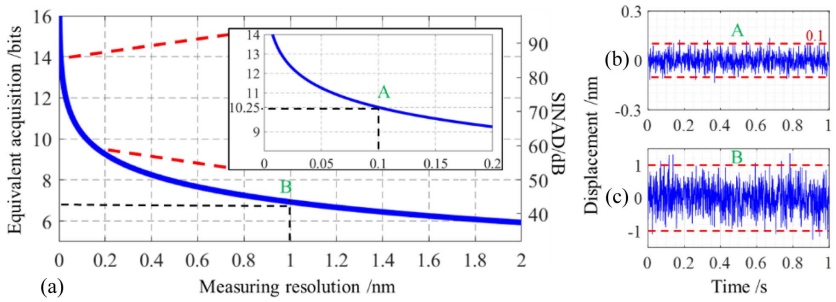

Fig. 3. (a) Relationship of displacement measuring resolution with equivalent acquisition bits and SINAD. (b), (c) Displacement measurement results around point A and point B, respectively, within 1 s.

carrier signals at the modulation frequency. They go through low-pass filters (LPFs) and become two orthogonal sine and cosine signals, denoted as u_1 and u_2, respectively. Subsequently, the two orthogonal signals are divided first and then the inverse tangent operation is performed to obtain the calculated phase, $\varphi'(t)$.

The PGC demodulation algorithm derives the output phase, $\varphi(t) = \arctan(u_1/u_2)$. The output error of the system, $\Delta\varphi(t)$, in the form of uncertainty, is evaluated as follows:

$$\Delta\varphi(t) = \sqrt{\left(\frac{\partial\varphi(t)}{\partial u_1}\cdot\Delta u_1\right)^2 + \left(\frac{\partial\varphi(t)}{\partial u_2}\cdot\Delta u_2\right)^2} = \sqrt{\left(\frac{u_2}{u_1^2+u_2^2}\right)^2\Delta u_1^2 + \left(\frac{u_1}{u_1^2+u_2^2}\right)^2\Delta u_2^2}, \quad (1)$$

where Δu_1 and Δu_2 are the errors of u_1 and u_2, respectively.

Since u_1 and u_2, obtained by analog-to-digital conversion within the solution system, originate from the same ADC, the resolution of the two signals is identical. Consequently, Δu_1 can be assumed to be equal to Δu_2. Through reasonable design, ignoring the errors introduced by CPD, AOIM, and filters, and when the phase modulation depth C is 2.63 [13], the amplitudes of the two signals, U_1 and U_2, are also equal. Utilizing the trigonometric function relationship, the output error of the system can be further simplified as follows:

$$\Delta\varphi(t) = \frac{\Delta u_1}{U_1}. \quad (2)$$

It can be observed that the final simplified expression of the phase error, $\Delta\varphi(t)$, is equivalent to the dynamic range of the output phase of the system.

According to Fig. 2, the solid green wireframe and solid yellow wireframe on the left correspond to ADC_1^* and ADC_2^*, marked by the dotted line frames of the corresponding colors on the right. Consequently, the entire interferometry and phase demodulation system can be regarded as two identical ADCs with the effective number of bits N^*, serving to convert analog displacement measurements to digital values. Existing displacement errors ΔL in the conversion process can be expressed as follows:

$$\Delta L = \frac{\lambda}{4\pi n}\Delta\varphi(t) = \frac{\lambda}{4\pi n}\cdot\frac{1}{2^{N^*}}. \quad (3)$$

The relationship between SINAD and N^* of the equivalent model can be expressed as follows:

$$N^* = \frac{\text{SINAD [dB]} - 1.76\text{ [dB]}}{6.02\text{ [dB]}}. \quad (4)$$

As shown in Fig. 3, equivalent acquisition bits and SINAD change with displacement measuring resolution can be derived from Eqs. (3) and (4). For instance, in an experiment utilizing a laser with a central wavelength of 1532.8 nm, the equivalent ADC resolution should be around 10.3 bits to achieve an interferometric accuracy of 0.1 nm. Hence, reasonable error distribution is required, offering guidance in the design of interference and calculation systems.

B. Analysis of Nonlinear Demodulation Error Mechanism at the Subnanometer Scale

According to the modulation and demodulation principle of FMI, the errors in the optical path are initially analyzed. First, there is a time delay τ between the laser output from the laser tube and the photodetector. Second, when the driving current modulates the frequency of the laser, it inevitably modulates the light intensity, causing the amplitude of the optical signal to periodically change according to the modulation frequency. These factors introduce nonlinear errors into the demodulation results. At this point, the interference signal i_m [23] can be represented as

$$\begin{aligned} i_m &= (1 + m\cos(\omega_0(t-\tau) + \varphi_m)) \\ &\quad\cdot(A + B\cos(C\cos(\omega_0(t-\tau)) + \varphi_0(t))) \\ &= (1 + m\cos(\omega_0 t - \varphi_\tau + \varphi_m)) \\ &\quad\cdot(A + B\cos(C\cos(\omega_0 t - \varphi_\tau) + \varphi_0(t))), \end{aligned} \quad (5)$$

where m represents the coefficient of AOIM; ω_0 is the modulation frequency; A is the DC component of the interference signal and B is the AC component of the interference signal; C is the depth of phase modulation; $\varphi_\tau = \omega_0\tau$ represents CPD due to the delay in the optical path; φ_m is the phase difference between AOIM and the laser center frequency modulation.

Upon analog-to-digital conversion, the quantization error of the detected interference signal emerges. By increasing the ADC bits to enhance the acquisition accuracy, the error can be minimized, so the effect of quantization error is ignored in this paper. Finally, during PGC demodulation, the interference signal is split into two paths. In practice, higher-order Bessel function expansions and mB related terms are ignored to achieve simplification due to lower impact. After the first

and second harmonic multiplication and filtering, the output results, u_1 and u_2, are expressed as

$$u_1 = -BJ_1(C\cos\varphi_\tau)J_0(C\sin\varphi_\tau)\cdot(1 + J_2(C\sin\varphi_\tau)/J_0(C\sin\varphi_\tau))\cdot\sin(\varphi_0(t)) + \frac{1}{2}mA\cos\Delta\varphi_{m\tau} + g(\omega_0), \tag{6}$$

$$u_2 = -BJ_2(C\cos\varphi_\tau)J_0(C\sin\varphi_\tau)\cdot\cos(\varphi_0(t)) + BJ_2(C\sin\varphi_\tau)J_0(C\cos\varphi_\tau)\cdot\cos(\varphi_0(t)) + h(\omega_0), \tag{7}$$

where J_0,J_1, and J_2 are zeroth-order, first-order, and second-order Bessel functions, respectively; $\Delta\varphi_{m\tau} = \varphi_m - \varphi_\tau$; $g(\omega_0)$ is the residual error after the first harmonic filter; $h(\omega_0)$ represents the residual error after the second harmonic filter.

Therefore, as illustrated in Fig. 4, the FMI demodulated by the PGC algorithm can be regarded as consisting of two data acquisition systems with multiplicative and additive error terms and an Arctan algorithm. After $\varphi_0(t)$ passes through ADC_1^* and ADC_2^*, the calculated phase $\varphi'(t)$ with errors can be determined by division and Arctan algorithms. The phase output result of the solution system is expressed as follows:

$$\varphi'(t) = \arctan\left(\frac{M_{m,\tau}\cdot M_{\tau1}\cdot\sin(\varphi_0(t)) + A_{m,\tau} + g(\omega_0)}{M_{\tau2}\cdot\cos(\varphi_0(t)) + A_{\tau2} + h(\omega_0)}\right), \tag{8}$$

where $M_{m,\tau}$ and $A_{m,\tau}$ are errors introduced by AOIM and CPD, which are multiplicative error and additive error, respectively. $M_{\tau1}$ and $M_{\tau2}$ are the multiplicative errors introduced by CPD. $A_{\tau2}$ is the additive error introduced by CPD into the cosine signal.

Therefore, the above errors can be briefly recorded as

$$\begin{cases} M_{m,\tau} = 1 + J_2(C\sin\varphi_\tau)/J_0(C\sin\varphi_\tau), \\ M_{\tau1} = -BJ_1(C\cos\varphi_\tau)J_0(C\sin\varphi_\tau), \\ M_{\tau2} = -BJ_2(C\cos\varphi_\tau)J_0(C\sin\varphi_\tau), \\ A_{m,\tau} = \frac{1}{2}mA\cos\Delta\varphi_{m\tau}, \\ A_{\tau2} = BJ_2(C\sin\varphi_\tau)J_0(C\cos\varphi_\tau)\cdot\cos(\varphi_0(t)). \end{cases} \tag{9}$$

Analyzing the influence of each error term on the measurement results.

(1) For terms $M_{\tau1}$ and $M_{\tau2}$, $|M_{\tau1}| = |M_{\tau2}|$ can be obtained when the value of $C\cos\varphi_\tau$ equals first- and second-order Bessel functions. Therefore, ideal solution results can be obtained by choosing a reasonable value of phase modulation depth C, while ignoring other error terms.

(2) However, there are some issues with the approach mentioned in (1). First, the same time delay τ will result in different carrier phase delays φ_τ at various modulation frequencies ω_0, so different C values need to be adjusted accordingly. Second, the error introduced by optical path delay only considers the multiplicative errors in (1), but additive error $A_{\tau2}$ cannot be avoided. Therefore, it is necessary to implement compensation measures to adapt $\omega_0\tau$. For instance, in the off-line compensation method, the average delay can be determined through several experiments, and an appropriate circuit delay can be introduced according to the value of ω_0, ensuring $\varphi_\tau = k\pi$, $k \in Z$. In the case of the online compensation method, delay effects can be eliminated by introducing an online compensation unit.

(3) For error terms $M_{m,\tau}$ and $A_{m,\tau}$, we can think of compensation methods in terms of $\Delta\varphi_{m\tau}$ or m. First, we can benefit from the phase compensation methods in (2), so that $\Delta\varphi_{m\tau} = \varphi_m - \varphi_\tau = (2k+1)\pi/2$, $k \in Z$, in order to eliminate the influence of $m\cos\Delta\varphi_{m\tau}$. Second, the effective approach is to design a light-intensity compensation system or establish a reference optical path to reduce the impact of the AOIM coefficient m on the solution system.

(4) Residual errors, $g(\omega_0)$ and $h(\omega_0)$, caused by the filters are due to the non-ideal nature of the LPF in the PGC algorithm. These errors result from spectrum aliasing and other factors. Hence, it is essential to design the attenuation coefficient and cutoff frequency of LPF reasonably to mitigate the influence of residual errors.

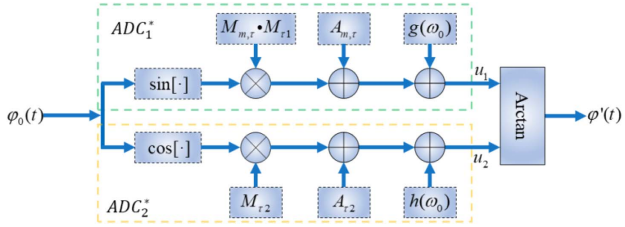

Fig. 4. Block diagram of resolution equivalent model including each error term.

4. HIGH-SPEED AND HIGH-PRECISION PGC DEMODULATION METHOD

A. Mechanism of PGC Demodulation Signal Blanking at High Speed and Large Ranges

After eliminating the errors caused by AOIM and PMD through existing techniques [16–20], this section then resolves the errors introduced by CPD in Eq. (5) under high-speed and long-distance measurement conditions. For the FMI, the essence of the motion of the object being measured is the Doppler shift. Therefore, the motion frequency of the object f_o can be equivalent to the motion speed v_o, as $f_o = 2v_o/\lambda$. The presence of a motion frequency induces a shift in the interference signal spectrum. Hence, when employing a certain modulation frequency, the spectrum of the interference signal shifts with the increasing motion speed of the measured object. If the speed continues to rise, spectrum aliasing occurs, ultimately rendering the interference demodulation system dysfunctional. It can be stated that the modulation frequency influences the theoretical maximum measurement speed that the interferometric system can demodulate. Considering a measurement speed index in this paper of 1.5 m/s, corresponding to a motion frequency of 2 MHz, the frequency of the modulating signal was finally selected as 10 MHz.

The impact of CPD on the equivalent acquisition bits and SINAD is examined using open-source numerical simulation software. As shown in Fig. 5, assuming that the object is in sinusoidal motion, Eq. (5) serves as the interference input signal, neglecting all other errors except for CPD, and the equivalent acquisition bits and SINAD are computed for various

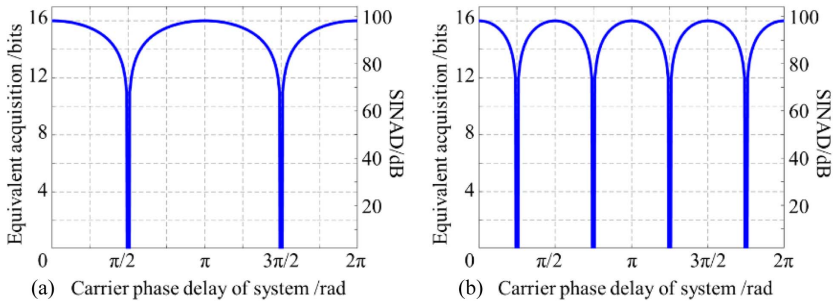

Fig. 5. Effect of CPD of the system on equivalent acquisition bits and SINAD. (a), (b) First and second harmonic demodulation signals, respectively.

CPDs, ranging from 0 to 2π. It can be observed that CPD exerts a substantial influence on the equivalent acquisition bits and SINAD of the first and second harmonics; particularly, when approaching odd multiples of $\pi/2$ or $\pi/4$, the equivalent acquisition bits and SINAD for the interference signal drop sharply, resulting in the inability to resolve the signal. Based on the previous analysis, increasing the carrier modulation frequency is essential to achieve high-velocity measurements, but it is inevitable that the CPD will increase significantly under the same system parameters. To delve further into this, certain assumptions are made. The modulation frequency of the carrier signal is set at 10 MHz, corresponding to a period of 100 ns. Consequently, the CPD of the light wave reaches 90 deg after a 1/4 period, which equals 25 ns. As a result, when conducting large-range measurements and measuring objects at varying distances, the corresponding CPD of the system as well as SINAD will be different.

The following simulation experiments were conducted to further elaborate on the requirements of large-range and high-velocity measurements. Figures 6(a) and 6(b) correspond to the variation of the equivalent acquisition bits and SINAD for the first and second harmonics with the work distance when the modulation frequency is 3 MHz, 7 MHz, and 10 MHz. Figures 6(c) and 6(d) correspond to the variation of the equivalent acquisition bits and SINAD for the first and second harmonics with the work distance when the initial delay angle is 0 deg, 45 deg, 90 deg, and 135 deg.

As shown in Figs. 6(a) and 6(b), it can be seen that for the requirement of low-speed measurement (corresponding to low modulation frequency), the equivalent acquisition bits and SINAD are not greatly affected by the variation of the work distance within the range of 2 m. However, as the measurement speed increases (the corresponding modulation frequency also increases), for example, when the modulation frequency is 10 MHz, the equivalent acquisition bits and SINAD of the second harmonics have huge errors at the work distance of about 1.9 m. The above analysis of the measurement speed shows that when the initial delay angle is zero and under

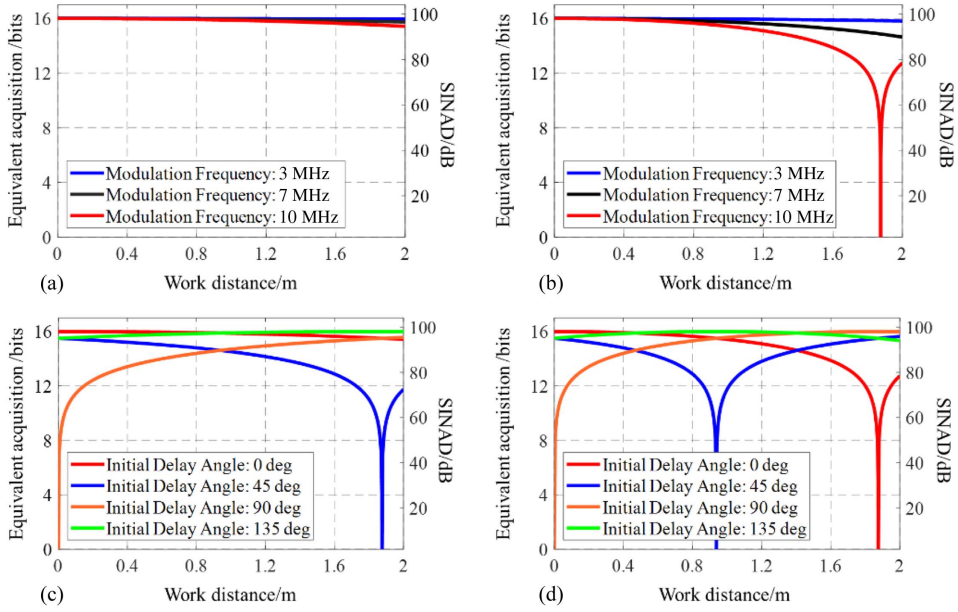

Fig. 6. Influence of modulation frequency and initial delay angle on equivalent acquisition bits and SINAD for work distance in the 2 m range. (a), (b) Variation curves of equivalent acquisition bits and SINAD for the first and second harmonic demodulation signals with the work distance when the modulation frequency is 3 MHz, 7 MHz, and 10 MHz. (c), (d) Variation curves of equivalent acquisition bits and SINAD for the first and second harmonic demodulation signals with the work distance when the initial delay angle is 0 deg, 45 deg, 90 deg, and 135 deg.

the same measurement conditions, the increase in the measurement speed also increases the CPD, which has a drastic effect. Then the effects of different initial delay angles when the modulation frequency is fixed will be studied below. As shown in Figs. 6(c) and 6(d), the modulation frequency is 10 MHz at this time. Compared with the curve when the initial delay angle is zero, it can be seen that when the initial phase keeps increasing, the error caused by the initial phase angle is directly superimposed on the error caused by the modulation frequency. In addition, the errors brought by different initial delay angles to the system are also different, and the initial delay angles in the actual experiments are also uncertain, which makes the errors caused by the initial delay angles difficult to avoid. Therefore, real-time dynamic adjustments of CPD are essential to ensure the accuracy and correctness of the demodulation results.

B. High-Precision PGC Demodulation Algorithm with Delay Dynamic Adaptive Regulation

Building on the previous analysis, there exists a carrier phase delay φ_τ between the interference signal and the internal reference signal, due to the time delay of $\tau = \tau_d + \tau_s$ after the interference signal passes through the detection optical path, where τ_d represents the time spent in the work distance, and τ_d is variable due to the object's motion. On the other hand, τ_s is the time taken by the other remaining optical paths (except the work distance), so it is a constant. During large-range measurements, the CPD progressively increases with the movement of the object, causing a decrease in the signal's SINAD after mixing, and it may even lead to the failure of the demodulation algorithm. Therefore, it is necessary to design a CPD compensation algorithm, which is divided into three stages.

First stage: when the object being measured has not started moving, and the system has just been powered on, a fixed CPD caused by circuit delay is generated. At this point, the CPD compensation amount of the reference signal generation module is adjusted up or down at fixed intervals. Simultaneously, the amplitude of the sinusoidal signal in the two orthogonal signals is monitored to determine whether it has reached its maximum. If the maximum is reached, the CPD compensation amount φ_s is locked at this time to complete the static CPD compensation.

Second stage: after the completion of static fixed CPD compensation, the measured object begins to move, and the CPD gradually increases with the motion of the object, resulting in a dynamic CPD. During this stage, the change in dynamic carrier phase delay φ_d can be calculated based on the phase information already demodulated by the PGC-Arctan algorithm. The dynamic carrier phase delay φ_d can be expressed as

$$\varphi_d = \omega_0 \tau_d = 2\pi f_0 \cdot \frac{2L}{c} = \frac{f_0}{v}\varphi'(t), \tag{10}$$

where f_0 is the laser modulation frequency; c is the speed of light in a vacuum; v is the output frequency of laser.

Third stage: the static CPD compensation φ_s from the first stage is added to φ_d, resulting in $\varphi_\tau = \varphi_d + \varphi_s$, which is then fed back to the CPD compensation input of the reference signal generation module to achieve real-time dynamic CPD compensation.

The experimental process depicted in Fig. 7 unfolds as follows. The DFB laser is current-modulated by the sinusoidal signal generated by the direct digital synthesis (DDS) unit and the digital-to-analog converter (DAC). The output light is transmitted through a single-mode fiber (SMF) and passes through the fiber isolator and the optical fiber circulator (OC). Then it travels through the GRIN lens and interferes, and then returns to the OC. The resulting interference signal enters the PGC demodulation system after passing through the ADC. At this point, both the static CPD caused by the circuit delay and the dynamic CPD arising from the motion of the object have been calculated and stored in the compensation algorithm. Following phase compensation, the first and second harmonic carrier signals are multiplied by the interference signals, followed by low-pass filtering. After dividing the two orthogonal signals, the inverse tangent operation is applied to obtain the phase to be measured, thus achieving phase demodulation.

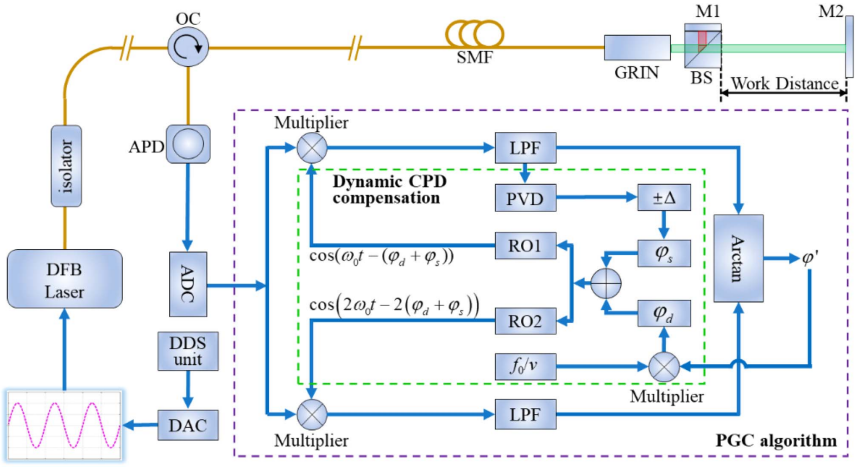

Fig. 7. High-speed and large-range PGC modulation and demodulation experimental device with dynamic CPD compensation. DDS unit: direct digital synthesis unit; DAC: digital-to-analog converter; DFB laser: distributed feedback laser; OC: optical fiber circulator; SMF: single-mode fiber; GRIN: gradient index lens; BS: beam splitting prism; M1: first reflector; M2: second reflector; APD: photodetector; PVD: peak value detection unit; ±Δ: variation of static CPD.

5. EXPERIMENTAL VALIDATION

In the experiment, a DFB laser serves as the dedicated laser source for the FMI, and it is driven by the DLC laser driver (DLC PRO, Toptica, Germany). The stable interference signal is detected by a photodetector and converted into a digital signal using a 16-bit ADC. The signal processing board is used for signal processing, as well as to generate sinusoidal modulated signals, which are output by a 14-bit DAC. The field programmable gate array (FPGA) is used to implement the PGC optimization algorithm, and the final demodulation results are subsequently sent to the personal computer via the universal serial bus (USB).

A. Validation of PGC Equivalent Resolution Model

To meet the requirements of equivalent signal acquisition accuracy for the phase-generated carrier demodulation lock-in amplifier unit mentioned earlier, a multi-functional programmable signal generator is set up. In order to measure the static measurement limit of the signal processing unit of the FMI, several steps were taken. The first step was to set $\varphi_0(t)$ as a fixed value in Eq. (5) to simulate the situation where the measured object was in a static state, and then connect the signal generated by the signal generator to the self-designed signal processing circuit board. The second step was to display the collected digital fluctuations of the first and second harmonics in Fig. 8. Figure 8(a) illustrates the test results of equivalent acquisition accuracy for the first harmonic lock-in amplifier, with the peak-to-peak value of equivalent digital quantity fluctuation being 24. Figure 8(b) shows the test result of equivalent acquisition accuracy for the second harmonic lock-in amplifier, with the peak-to-peak value of equivalent digital quantity fluctuation being 25. According to the relation between digital fluctuation and equivalent acquisition bits, the equivalent acquisition accuracies for the first and second harmonic lock-in amplifiers are 11.42 bits and 11.36 bits, respectively. These values are close to each other and align with the assumption made in Section 2 regarding signal processing accuracy analyses. Furthermore, both values are better than 10.30 bits, proving that the unit design can meet the requirements of 0.1 nm displacement measuring resolution.

The experiments conducted above confirm that the phase-generated carrier demodulation unit meets the requirements of subnanometer resolution design. The third step was to test the accuracy of the carrier demodulation generated by the phase-generated carrier lock-in amplifiers combined with the arctan unit, as shown in Fig. 9. The signal demodulation output of the FMI is collected over 3 h, completing the long-term static phase test of the system. According to the test results, the peak-to-peak value fluctuation of the digital quantity is eight, and the corresponding displacement and jitter amount is less than 0.1 nm.

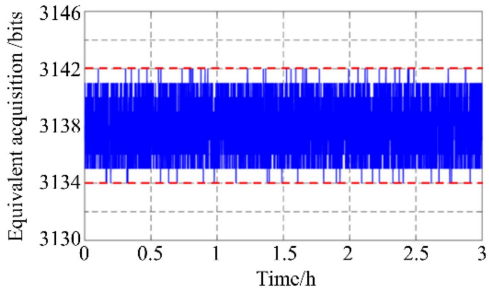

Fig. 9. Phase static noise test of the signal demodulation system.

B. Validation of PGC Dynamic CPD Compensation Method

On the basis of previous analyses, it is evident that CPD changes two orthogonal signals with equal amplitude into orthogonal signals with different amplitudes, thereby directly impacting the demodulation of SINAD. In the context of a large range and high measurement velocity, the CPD rises with the increasing displacement of the object being measured. The CPD compensation module can be verified by comparing the two amplitude ratios of the two orthogonal signals before and after compensation. The following specific steps were taken. First, a programmable signal generator was employed to generate an analog interference signal with the object to be measured in a constant motion state and with a dynamic CPD change. The signal was then transmitted to the demodulation system, and the data of the two pairs of orthogonal signals before and after CPD compensation were collected. As demonstrated in Fig. 10, a comparison was made between the results measured by the proposed method and the methods described in previous research [24,25] through experiments.

Figure 10(a) explores the relationship between the calculated carrier phase delay φ_τ' and the phase to be measured φ_0. Analysis reveals that the blue curve, representing the former research method [24], exhibits spikes at certain specific points. This occurs because when φ_0 is $k\pi$, $k \in Z$, the value obtained by dividing the sine and cosine signals is either zero or infinite, so an accurate carrier phase delay value cannot be obtained.

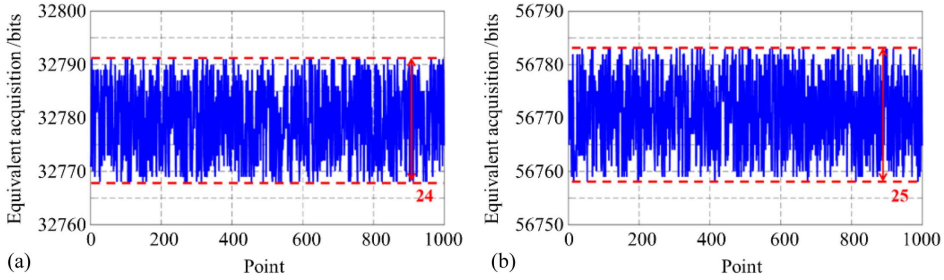

Fig. 8. Static test of equivalent acquisition accuracy of the phase-generated carrier lock-in amplifiers. (a), (b) Equivalent test results for the primary and secondary channels, respectively.

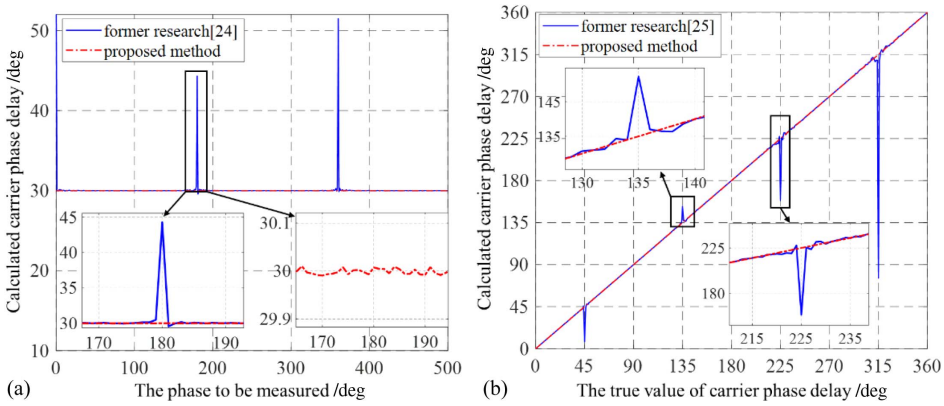

Fig. 10. Comparison of CPD compensation effects of different demodulation methods. (a) Comparison of the influence of the phase to be measured φ_0 on the carrier phase delay $\varphi_{\tau'}$ calculated by the former research method and the proposed method. (b) Comparison of the calculated carrier phase delay $\varphi_{\tau'}$ with the true value of carrier phase delay φ_τ using the former research method and the proposed method.

Conversely, by observing the red curve representing the proposed method, it can be observed that $\varphi_{\tau'}$ remains unaffected by the change in φ_0. Second, the $\varphi_{\tau'}$ was compared to the true value of the carrier phase delay, φ_τ [Fig. 10(b)]. It was found that when φ_τ is $(2k+1)\pi/4$, $k \in Z$, the blue curve, representing the method of former research [25], also exhibits spikes. This happens because the presence of CPD introduces a multiplicative error term $\cos(2\varphi_\tau)$ in the cosine signal, leading to the denominator term in the division signal under these specific points becoming zero. Consequently, an accurate carrier phase delay value cannot be obtained. In contrast, the red curve, representing the proposed method, indicates that $\varphi_{\tau'}$ is consistent with φ_τ and remains unaffected by φ_τ.

In summary, when φ_0 and φ_τ take certain specific points, the former research methods yield error-prone results with significant errors, resulting in inaccurate CPD compensation values. In contrast, the results calculated by the proposed method are accurate and unaffected by these specific points.

C. Experimental Verification of Subnanometer Resolution and High-Speed Measurement of FMI

Resolution measurement experiments were conducted using a programmable signal generator to generate an analog interference signal with the step motion state of the object to be measured. Various bit step values, 0.36 nm, 0.20 nm, 0.15 nm, and 0.10 nm, were set. The results obtained are displayed in Fig. 11.

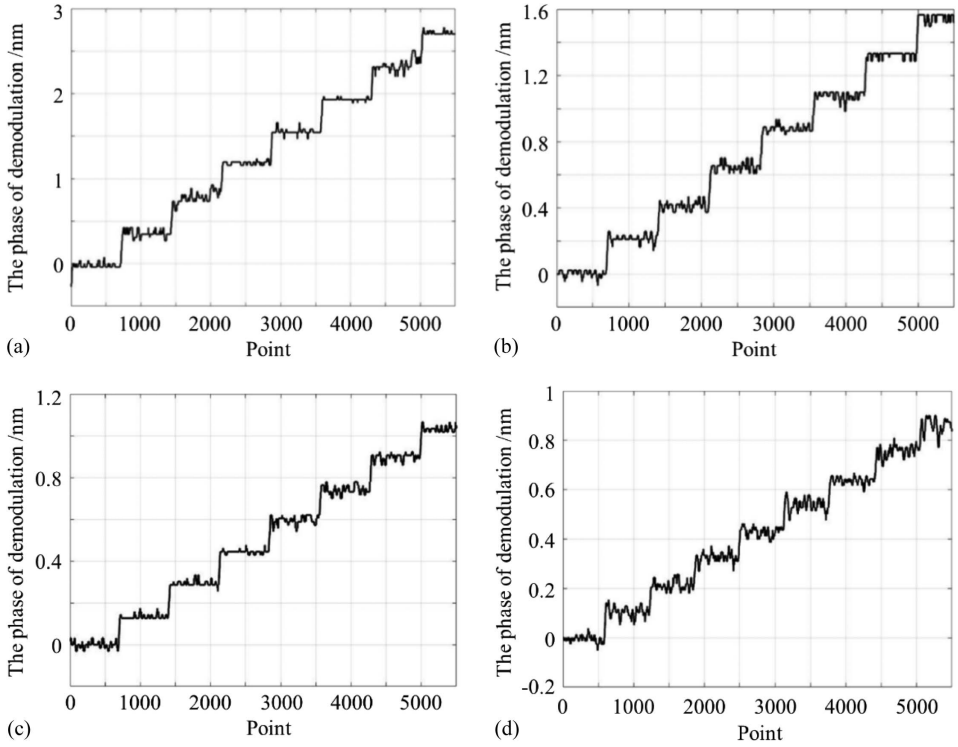

Fig. 11. Electrical test results of the displacement measuring resolution of the demodulating system. (a) 0.36 nm, (b) 0.20 nm, (c) 0.15 nm, and (d) 0.10 nm.

It can be observed that the steps are clear and distinguishable, indicating that the electrical test resolution of the measuring system is 0.10 nm.

As shown in Fig. 12, experiments were conducted to measure the speed of the system. A programmable signal generator was used to generate an interference signal simulating the uniform motion state of the measured object at speeds of 383.2 mm/s, 766.4 mm/s, 1149.6 mm/s, and 1532.8 mm/s. The collected data after demodulation were uploaded to the computer for the least squares fitting. A total of 4096 collected points were selected for data fitting, and the fitting results under different speeds were obtained.

Figure 13 illustrates the results of displacement residuals at speeds of 383.2 mm/s, 766.4 mm/s, 1149.6 mm/s, and 1532.8 mm/s. As observed from the figure, the residual increases with the increasing object's motion speed. This is attributed to the increase in the motion frequency of the object to be measured, which broadens the spectrum of the interference signal, ultimately reducing the stopband attenuation of the low-pass filter.

The displacement standard deviation was calculated based on the fitting results and the residual distribution. The relationship between the standard deviation of measurement and the frequency of motion is plotted in Fig. 14.

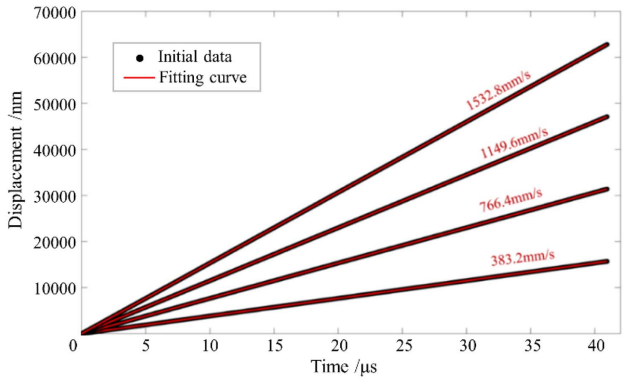

Fig. 12. Fitting results at speeds of 383.2 mm/s, 766.4 mm/s, 1149.6 mm/s, and 1532.8 mm/s.

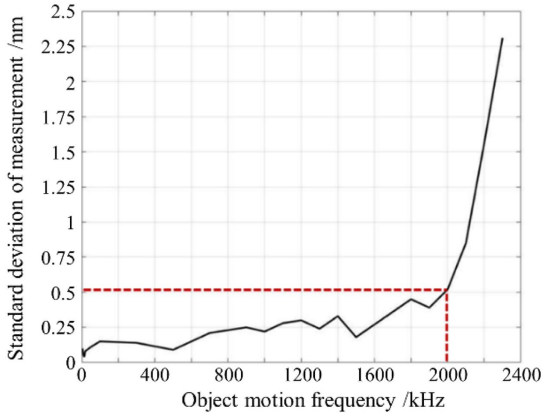

Fig. 14. Relationship between standard deviation of measurement and motion frequency.

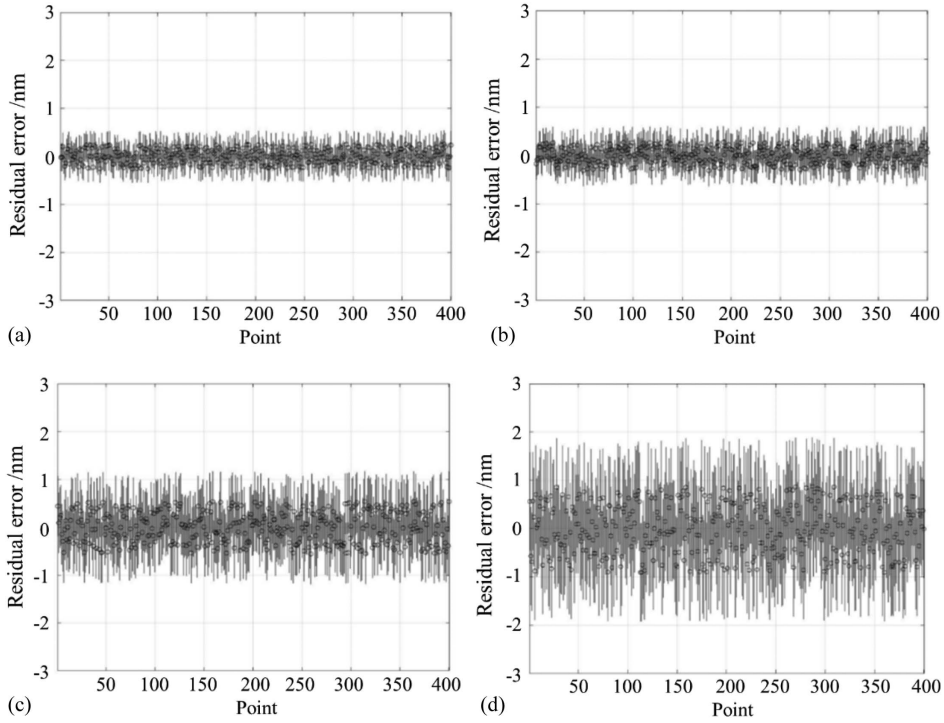

Fig. 13. Results of measurement velocity residual of the demodulating system at speeds of (a) 383.2 mm/s, (b) 766.4 mm/s, (c) 1149.6 mm/s, and (d) 1532.8 mm/s.

It reveals that when the equivalent frequency of the motion of the object to be measured is within the range of 2000 kHz, that is, when the motion speed of the object to be measured is within 1.5 m/s, the measurement standard deviations are consistently below 0.5 nm. This shows that the demodulation system has achieved subnanometer precision at a high-speed measurement of 1.5 m/s.

6. CONCLUSIONS

The new generation of ultra-precise FMI plays a vital role in displacement measurement with subnanometer resolution, thanks to its advantages of compact measurement space and high integration. Phase-generated carrier demodulation technology based on internal modulation is a commonly used phase demodulation method. However, this algorithm is only suitable for small distance and low-speed measurement conditions, and nonlinear errors are introduced under high-speed and large-range modulation.

This paper proposes, for the first time, a resolution equivalent model, which equivalently models the modulation and PGC demodulation processes as a signal acquisition system, enabling the total error generated by all internal links to be characterized using N^* in the resolution equivalent system, providing a basis for error allocation in subnanometer resolution design. Additionally, this paper offers a theoretical analysis of nonlinear errors and error sources generated during high-speed measurement. It presents an adaptive compensation algorithm combining both dynamic and static CPD to address the errors introduced by CPD during PGC demodulation. Experimental results demonstrate that when the measurement speed is 1.5 m/s, the measurement error caused by CPD can be reduced to less than 0.5 nm, thus achieving subnanometer resolution accuracy requirements.

In the future, we aim to further analyze other error sources presented here and provide practical solutions to enhance measurement accuracy.

Funding. National Key Research and Development Program of China (2022YFF0705802); Natural Science Foundation of Heilongjiang Province (LH2019E048); China Postdoctoral Science Foundation (2023M730883); National Postdoctoral Program for Innovative Talents (BX20230478).

Disclosures. The authors declare no conflicts of interest.

Data Availability. Data underlying the results presented in this paper are not publicly available at this time but may be obtained from the authors upon reasonable request.

REFERENCES

1. H. Chen, X. Ding, Z. Zhong, *et al.*, "High acceleration ultra-precision measurement model in laser heterodyne interferometry," Opto-Electron. Eng. **34**, 72–75 (2007).
2. W. Gao, S. Kim, H. Bosse, *et al.*, "Measurement technologies for precision positioning," CIRP Ann. **64**, 773–796 (2015).
3. G. Schitter, J. Steininger, F. C. Heuck, *et al.*, "Towards fast AFM-based nanometrology and nanomanufacturing," Int. J. Nanomanuf. **8**, 392–418 (2012).
4. J. Watchi, S. Cooper, B. L. Ding, *et al.*, "Contributed review: a review of compact interferometers," Rev. Sci. Instrum. **89**, 18–26 (2018).
5. H. Nozato, W. Kokuyama, and A. Ota, "Improvement and validity of shock measurements using heterodyne laser interferometer," Measurement **77**, 67–72 (2016).
6. X. Zhou and Q. Yu, "Wide-range displacement sensor based on fiber-optic Fabry–Perot interferometer for subnanometer measurement," IEEE Sens. J. **11**, 1602–1606 (2011).
7. Q. Wang and Z. Ma, "Feedback-stabilized interrogation technique for optical Fabry–Perot acoustic sensor using a tunable fiber laser," Opt. Laser Technol. **51**, 43–46 (2013).
8. X. Mao, X. Zhou, and Q. Yu, "Stabilizing operation point technique based on the tunable distributed feedback laser for interferometric sensors," Opt. Commun. **361**, 17–20 (2016).
9. A. Dandridge, A. B. Tveten, and T. G. Giallorenzi, "Homodyne demodulation scheme for fiber optic sensors using phase generated carrier," IEEE J. Quantum Electron. **18**, 1647–1653 (1982).
10. T. R. Christian, P. A. Frank, and B. H. Houston, "Real-time analog and digital demodulator for interferometric fiber optic sensors," Proc. SPIE **2191**, 324–336 (1994).
11. Y. Dong, P. Hu, M. Ran, *et al.*, "Phase modulation depth setting technique of a phase-generated-carrier under AOIM in fiber-optic interferometer with laser frequency modulation," Opt. Express **28**, 31700–31713 (2020).
12. J. He, L. Wang, F. Li, *et al.*, "An ameliorated phase generated carrier demodulation algorithm with low harmonic distortion and high stability," J. Lightwave Technol. **28**, 2912–2918 (2010).
13. L. Yan, Y. Zhang, J. Xie, *et al.*, "Nonlinear error compensation of PGC demodulation with the calculation of carrier phase delay and phase modulation depth," J. Lightwave Technol. **39**, 2327–2335 (2021).
14. B. Chen, J. Jiang, Y. Lou, *et al.*, "Active linearized PGC demodulation with fusion of PGC-Arctan and PGC-DCM schemes for nonlinear error elimination in SPM interferometer," Opt. Express **30**, 22999–23010 (2022).
15. Y. Li, H. Gao, L. Zhao, *et al.*, "Improved PGC demodulation algorithm to eliminate modulation depth and intensity disturbance," Appl. Opt. **61**, 5722–5727 (2022).
16. Z. Qu, S. Guo, C. Hou, *et al.*, "Real-time self-calibration PGC-Arctan demodulation algorithm in fiber-optic interferometric sensors," Opt. Express **27**, 23593–23609 (2019).
17. L. Yan, Z. Chen, B. Chen, *et al.*, "Precision PGC demodulation for homodyne interferometer modulated with a combined sinusoidal and triangular signal," Opt. Express **26**, 4818–4831 (2018).
18. A. V. Volkov, M. Y. Plotnikov, M. V. Mekhrengin, *et al.*, "Phase modulation depth evaluation and correction technique for the PGC demodulation scheme in fiber-optic interferometric sensors," IEEE Sens. J. **17**, 4143–4150 (2017).
19. S. Zhang, Y. Chen, B. Chen, *et al.*, "A PGC-DCDM demodulation scheme insensitive to phase modulation depth and carrier phase delay in an EOM-based SPM interferometer," Opt. Commun. **474**, 126183 (2020).
20. A. Zhang and D. Li, "Interferometric sensor with a PGC-AD-DSM demodulation algorithm insensitive to phase modulation depth and light intensity disturbance," Appl. Opt. **57**, 7950–7955 (2018).
21. C. Ni, M. Zhang, Y. Zhu, *et al.*, "Sinusoidal phase-modulating interferometer with ellipse fitting and a correction method," Appl. Opt. **56**, 3895–3899 (2017).
22. J. Shi, D. Guang, S. Li, *et al.*, "Single-wavelength passive phase-shifted demodulation technique with the dual-cavity and EFA for the interrogation of EFPI diaphragm-based fiber sensor," J. Lightwave Technol. **40**, 222–227 (2022).
23. Y. Dong, P. Hu, H. Fu, *et al.*, "Long range dynamic displacement: precision PGC with subnanometer resolution in an LWSM interferometer," Photon. Res. **10**, 59–67 (2022).
24. K. Wang, M. Zhang, F. Duan, *et al.*, "Measurement of the phase shift between intensity and frequency modulations within DFB-LD and its influences on PGC demodulation in a fiber-optic sensor system," Appl. Opt. **52**, 7194–7199 (2013).
25. J. Xie, L. Yan, B. Chen, *et al.*, "Extraction of carrier phase delay for nonlinear errors compensation of PGC demodulation in an SPM interferometer," J. Lightwave Technol. **37**, 3422–3430 (2019).